



Chronology of the cave interior sediments at Gran Dolina archaeological site, Atapuerca (Spain)



J.M. Parés ^{a,*}, C. Álvarez ^a, M. Sier ^{b,c,d}, D. Moreno ^a, M. Duval ^e, J.D. Woodhead ^f, A.I. Ortega ^{a,g}, I. Campaña ^a, J. Rosell ^{h,i}, J.M. Bermúdez de Castro ^{a,j}, E. Carbonell ^{h,i}

^a CENIEH, Paseo Sierra de Atapuerca 3, 09002 Burgos, Spain

^b Department of Earth Sciences, Oxford University, South Parks Road, OX1 3AN Oxford, United Kingdom

^c Paleomagnetic Laboratory Fort Hoofddijk, Faculty of Geosciences, Utrecht University, 3584 CD, Utrecht, The Netherlands

^d Faculty of Archaeology, Leiden University, PO Box 9515, 2300 RA, Leiden, The Netherlands

^e Australian Research Centre for Human Evolution, Environmental Futures Research Institute, Griffith University, 170 Kessels Road, Nathan, Australia

^f School of Earth Sciences, University of Melbourne, VIC, 3010, Australia

^g Fundación Atapuerca, Ctra. de Logroño, 44, 09198 Ibeas de Juarros, Spain

^h Institut Català de Paleoecologia Humana i Evolució Social, c/ Marcelí Domingo s/n, Campus Sesceletes, 43007 Tarragona, Spain

ⁱ Area de Prehistoria, Dept. d'Història de l'Art, Univ. Rovira i Virgili, Fac. de Lletres, Av. Catalunya, 35, 43002 Tarragona, Spain

^j Department of Anthropology, University College London, 14 Taviton Street, London, WC1H 0BW, UK

ARTICLE INFO

Article history:

Received 29 September 2017

Received in revised form

31 January 2018

Accepted 6 February 2018

ABSTRACT

The so-called “Gran Dolina site” (Atapuerca mountain range, N Spain) is a karstic cavity filled by sediments during the Pleistocene, some of which contain a rich ensemble of archaeological and paleontological records. These sediments have contributed significantly to our understanding of early human dispersal in Europe but, in contrast, older, interior facies deposits have received much less of attention. The stratigraphy of Gran Dolina reveals an abrupt sedimentary change of interior to entrance facies from bottom to top, reflecting a significant paleoenvironmental change that promoted the accumulation of sediments transported from the vicinity of the cave by water or “en masse”. Since the major magnetic polarity reversal known as the Matuyama-Brunhes boundary (0.78 Ma) was detected within the TD7 unit in the middle of the stratigraphic section, we carried out a new combined paleomagnetic, radiometric (U-Pb), and electron spin resonance (ESR) dating study of the lower part of the sequence in order to constrain the chronology of the interior facies at Gran Dolina. U-Pb analysis of speleothems did not produce age information as the samples proved to be extremely unradiogenic. The magnetic stratigraphy of the cave interior sediments reveals a dominant reverse magnetic polarity, coherent with a Matuyama age, and interrupted by a normal polarity magnetozone interpreted as the Jaramillo Subchron (1.0–1.1 Ma). ESR ages on quartz grains from the upper part of the interior facies sediments are coherent with such an interpretation. We conclude that the fluvial deposits (interior facies) that constitute the cave floor began accumulating before 1.2 Ma. The development of large cave entrances at Gran Dolina occurred shortly after the Jaramillo Subchron but before ca 900 ka ago.

© 2018 Elsevier Ltd. All rights reserved.

1. Introduction

Research at the Lower Paleolithic cave site of Gran Dolina, Sierra de Atapuerca (northern Spain) (Fig. 1), has led to major advances in our understanding of human evolution and occupation of Eurasia in the Pleistocene. The Gran Dolina site has produced thousands of

fossils and artifacts since 1995, when the first hominin remains were reported, and soon became a Pleistocene landmark in studies of early human settlement outside the African continent (Carbonell et al., 1995, 2008). Stratigraphic layer TD6 of Gran Dolina has yielded over 170 human fossil remains, more than 200 lithic artifacts, classified as Mode 1, as well as several thousand small and large vertebrate remains (Bermúdez de Castro et al., 1997; Carbonell et al., 2005; Bermúdez de Castro et al., 2008; Ollé et al., 2013). The initial paleomagnetic dating at Gran Dolina revealed a switch from reverse to normal geomagnetic polarity above TD6 level,

* Corresponding author.

E-mail address: josep.pares@cenieh.es (J.M. Parés).

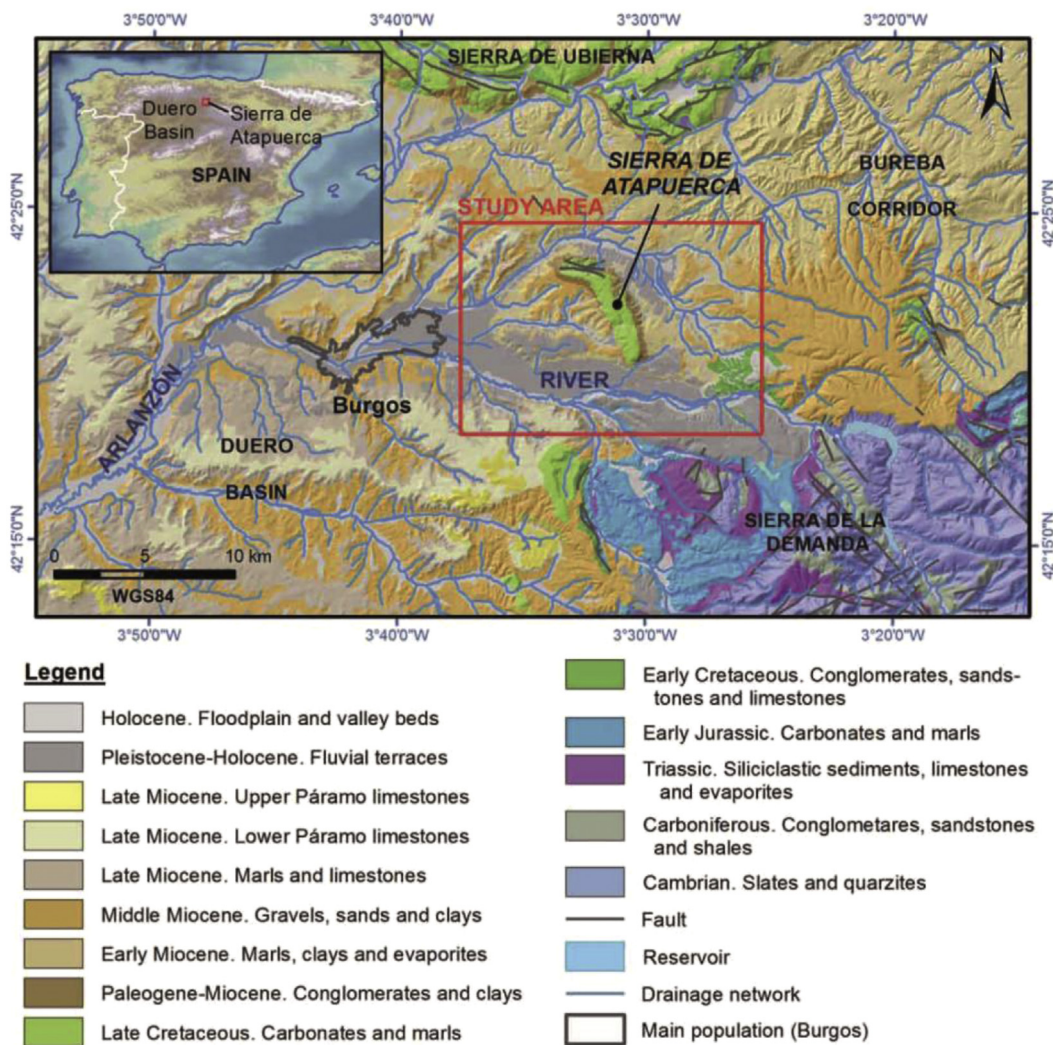


Fig. 1. Regional geological map of the study area showing the main lithological units (above), and a 3D view of the Atapuerca Mountain Range (Benito-Calvo and Pérez-González, 2015).

interpreted as the Matuyama-Brunhes boundary (MBB), providing a minimum age of 0.78 Ma for the archaeo-paleontological layer TD6 (Parés and Pérez-González, 1995). Subsequent chronometric analysis by Electron Spin Resonance (ESR) and luminescence further reinforced the paleomagnetic age (Falguères et al., 1999), and currently an age of around 0.85 Ma is accepted for the TD6 level (Parés et al., 2013; Arnold et al., 2014; Moreno et al., 2015). About four meters below TD6, stratigraphic layer TD4, a breccia of gravel-size clasts in a muddy and sandy matrix, is known to contain archaeological artifacts although no human fossils have been found yet (Carbonell and Rodríguez, 1994) (Fig. 2). The chronology of the ensemble TD4-TD5 levels is constrained by ESR dates on quartz grains and ranges between 0.9 and 1.13 Ma (Moreno et al., 2015). Such an age range overlaps with the Jaramillo Subchron (1.00–1.07 Ma) and therefore paleomagnetism allows testing whether level TD1 has a pre or post-Jaramillo age and in doing so constraining the age of the overlying, lithic-tool bearing layer TD4. Due to the progress of the excavation during the past five years, it has recently been possible to reach the bottom of TD1 stratigraphic layer at Gran Dolina, extending by ten more meters the current stratigraphic profile at the site.

There is very little chronological constraint on the underlying interior cave deposits that make up layer TD1. Interior facies deposits in caves are found in parts that are more remote and far the cave entrance, in total darkness, and typically in the vadose and upper phreatic zone of the cave system. Deposition modes in such areas are determined by the hydrologic conditions and may consist of fluvial gravels, sands and clays, commonly referred as fluvial facies. Even though layer TD1 is sterile, a better age for the sediments would constitute a maximum age for the overlying archaeological layer. Since the MB boundary has been identified in TD7, TD1 is known to be older than 0.78 Ma (Parés et al., 2013). The only direct ages available so far are based on ESR dating of optically bleached quartz grains extracted from the top of TD1. The three samples dated by Moreno et al. (2015) confirm an Early Pleistocene chronology, but the age scatter (from 789 ± 61 to 1249 ± 126 ka) does not provide any further age constraint. In this study we report new paleomagnetic and ESR dating results from cave interior sediments layer TD1, well below the fossiliferous stratigraphic units, and well below the MB boundary recorded in TD7/TD8. Such new chronological constraints will build on the existing chronology in two different ways. First, paleomagnetism can detect the presence of subchrons along the Gran Dolina lower section in TD1 that could help establishing additional time lines in the sedimentary infill. For this purpose we collected numerous paleomagnetic samples through 9 m in layer TD1, including laminated clastic deposits that preceded the opening of large entrances to the cave and the concomitant accumulation of fossils and artifacts. Second, we re-analysed with ESR three quartz samples from the bottom of the sedimentary sequence that were previously dated by Moreno et al. (2015), by measuring the Ti-center and by obtaining new dose rate measurements. Last, we attempted to date two flowstones at the top of TD1 with the U-Pb method.

2. Geological setting

At first glance the Gran Dolina sedimentary deposits reveal a rather common succession in karstic tiered caves that developed in relation to progressive river incision. Passages of phreatic origin form at or just below the water table and are subjected to frequent flooding and associated deposition of slackwater deposits by stream flows. Accumulation of drip-type flowstones such as stalactites and stalagmites will often cap the fine clastic sediments, although these can also form after groundwater draining. In either case, the development of flowstones in caves has been associated

with prolonged valley stability (e.g., Frank et al., 2006; Couchoud, 2008; Harmand et al., 2017). As incision lowers the local water table such passages are progressively abandoned and subjected to truncation by valley deepening, collapse, or fissuring that eventually will lead to the formation of a cave entrance. Talus, slope wash, and sliding bed mode deposits will then accumulate at the cave entrance and up to several meters in to the cave. Such processes will produce a variety of gravel accumulation, diamictons, and channel facies, controlled by water availability and particle size (e.g., Bosch and White, 2004). The Gran Dolina stratigraphy has been divided into 12 main units termed TD1 to TD 11 from bottom to top (Campaña et al., 2017). It reflects a broad evolution and includes cave interior deposits at the bottom (including both silts, clays and flowstones) below TD4 unit, and an assemblage of diamictons and gravels often showing channel cut-and-fill structures with abundant sand and silts from TD4 to the top of the sequence (Fig. 2). Cave entrance deposits will not be further considered in this paper and details can be found in Campaña et al. (2017). Below a prominent flowstone at the base of these cave entrance deposits (the basal “stalagmitic crust” of Carbonell and Rodríguez, 1994), the sedimentary record is mostly made up by silts and clays of fluvial origin (Fig. 2). Although a detailed study of such sediments is underway, the source of these cave interior sediments likely includes fluvial deposits and filtrates from soils (terra rossa). Silts and clays are often laminated, a quite common feature in phreatic environments (e.g., Ford and Williams, 2007), although the presence of two flowstones towards the top of the section suggests sporadic proximity to the vadose zone. The lower half of the stratigraphic section is characterized by a conspicuous unit of inclined laminar bedding silts and clays. Laminae are parallel to the depositional surface and therefore the unit corresponds to parallel accretion (Bull, 1981), so deposition of silt and clay laminae that are concordant to the underlying bedrock topography. Locally, such laminated silts and clays form couplets (3–4 cm thick), possibly suggestive of frequent flooding and drawing (Ford and Williams, 2007) by a mechanism linked to climatic events.

Consequently, our sampling was focused on the cave interior deposits TD1-TD2, which basically correspond to a slackwater facies and the capping flowstones, with the ultimate goal of extending the magnetostratigraphy at Gran Dolina to the floor of the cavity. In addition to this 9 m-thick new profile (hereafter called the Vicho section), a shorter one (South Trench) 4 m south and encompassing the layers sampled for ESR was also sampled and paleomagnetically studied and the description can be found somewhere else (Campaña et al., 2017).

3. Sampling and procedures

3.1. Paleomagnetism and rock-magnetism

Owing to the cementation of the cave deposits, two different methods have been used to obtain paleomagnetic samples. In flowstones and cemented siltstones we used a gas-powered drilling machine, equipped with a 1-inch non-magnetic drill bit. Soft, non-cohesive clay and silt deposit samples were obtained by pushing standard 8 cm^3 cubic or cylindrical plastic boxes into a clean, vertical surface. In both cases orientation of the specimens was performed *in situ* using a standard orientation device (compass-inclinometer) to obtain the azimuth and dip of the samples. Paleomagnetic analyses were carried out at the Geochronology facilities at the CENIEH (Burgos, Spain). Measurement of the natural remanent magnetization (NRM) of the samples was performed with a cryogenic magnetometer 2G model 755R–4K, which includes an online AF degausser capable of producing a peak field of 170 mT. Thermal demagnetization of the NRM was carried out with

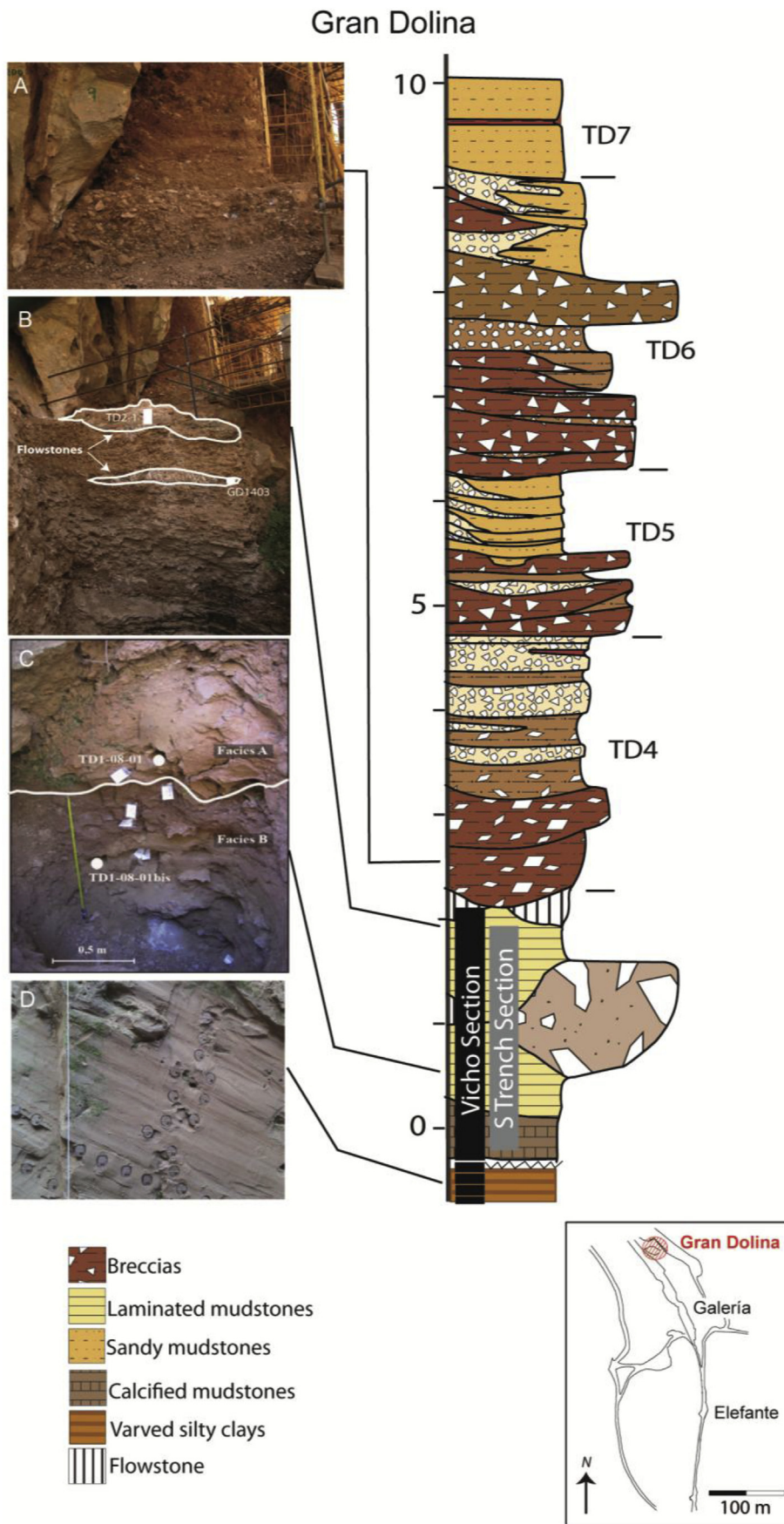


Fig. 2. Gran Dolina sedimentary infill above the interior facies (units TD4 to lower part of TD7). Photographs: A- Breccias of the lower part of unit TD4; B- Speleothems at the top of unit TD1 and location of samples for U-Pb analysis (see text for details); C- Position of the three ESR samples in S Trench section; D- Detail of laminated silty clays in the lower part of the interior facies deposits. Location of the two studied sections is shown at the bottom of the stratigraphic column (Vicho Section and S Trench Section). Facies and stratigraphic section modified from Campaña et al. (2017). Insert shows the general context of the Gran Dolina site on a map view of the excavation area.

an oven (model TD-48, ASC Scientific). Standard orthogonal, Zijderveld-type plots were used to interpret the structure of remanence components to later computing the direction of the Characteristic Remanent Magnetization (ChRM) directions using linear regression, guided by visual inspection of orthogonal demagnetization plots. Rockmagnetic analysis included hysteresis cycles, which were obtained on a 3900 VSM MicroMag (Princeton).

For sedimentary fabric characterization, we have used the anisotropy of magnetic susceptibility (AMS). The low field magnetic susceptibility of a rock (the ratio of magnetization, M , to the applied field H , or $K = M/H$) is given by the total contribution of its bulk mineralogy, including paramagnetic (e.g., phyllosilicates, iron-bearing feldspars), diamagnetic (e.g., quartz, calcite) and ferromagnetic (*sensu lato*; e.g., magnetite, goethite, hematite) grains. The AMS is defined by an ellipsoid (Nye, 1957) whose semi-axes are the three principal susceptibilities ($K_{\max} \geq K_{\text{int}} \geq K_{\min}$). AMS in siliciclastic rocks depends mostly on the crystallographic preferred orientation of the individual components, mostly phyllosilicates, and compositional layering. Therefore, AMS can be used as a proxy for grain preferred orientation in a variety of rocks (e.g., Tarling and Hrouda, 1993). Some of the advantages of using AMS as opposed to x-ray, or other methods such as neutron diffraction are the speed of the measurement and the integration of thousands of grains as analyses are performed on several cubic centimeters of rock at a time.

AMS was measured on a 1-FA Kappabridge (AGICO Instruments), a fully automated inductive bridge, at a frequency of 976 Hz and with a field of 200 A/m. The measurement takes about 2 min per specimen and is very precise, due to many susceptibility determinations in each plane perpendicular to the axis of specimen rotation. The errors in determination of this tensor are estimated using a method based on multivariate statistics principles Jelinek (1978). There is a plethora of parameters to describe the axial magnitude relationships of the susceptibility ellipsoid (see also Tauxe, 1993; Tarling and Hrouda, 1993). The simplest expressions are the axial ratios L (K_{\max}/K_{int}) (Balsley and Buddington, 1960), F (K_{int}/K_{\min}) (Stacey et al., 1960) and P (K_{\max}/K_{\min}) (Nagata, 1961). Alternatively, other authors use the parameters P' ($P' = \exp(2(a_1^2 + a_2^2 + a_3^2))^{1/2}$) (Jelinek, 1981) where $a_1 = \ln(K_{\max}/K_b)$, etc.

and $K_b = (K_{\max} + K_{\text{int}} + K_{\min})/3$ (Nagata, 1961) to express the fabric intensity as a measure of eccentricity and T ($T = 2(\ln K_{\text{int}} - \ln K_{\min}) / [\ln K_{\max} - \ln K_{\min}] - 1$) (Jelinek, 1981) to define the degree to which the ellipsoid is oblate or prolate, both adopted in this study.

3.2. Electron spin resonance of optically bleached quartz grains

Among the 39 quartz samples previously ESR dated at Gran Dolina by Moreno et al. (2015), three of them (TD1-08-01bis, TD1-08-01 and TD1-08-02) were taken from the upper part of level TD1 layer and are consequently of direct interest for the present study. Full details of the sample preparation, gamma irradiations and laboratory bleaching experiment can be found in Moreno et al. (2015). All the aliquots (i.e., gamma-irradiated, natural and bleached aliquots) of these three quartz samples were re-measured by ESR using the experimental setup at CENIEH (see details in Duval and Guilarte Moreno, 2012) and following the most advanced analytical procedures as in Duval et al. (2017). New *in situ* gamma spectrometry measurements were also carried out at the exact sampling spots with a NaI probe connected to an Inspector1000 multichannel analyzer (Canberra).

In accordance with the Multiple Centre (MC) approach, the ESR signals of both the Al and Ti centres using experimental conditions as in Duval et al. (2017). When possible, the angular dependence of the ESR signal due to sample heterogeneity was taken into account by measuring each aliquot three times after a ~120° rotation in the cavity. However, only one angle of each aliquot was measured for the ESR signal of the Ti centres in samples TD1-08-01 and TD1-08-02 because of the weak ESR intensities that required to significantly increase the number of scans (10–25 scans here) for one given measurement. This resulted in a total measurement time >3 h for a given sample. Beyond this duration the stability of the experimental setup might become an issue and impact the repeatability of the measurements (Duval and Guilarte Moreno, 2012). Furthermore, data reproducibility was checked by running repeated ESR measurements over different days. The ESR intensities of Al and Ti centres were extracted and corrected as in Duval et al. (2017). Following Duval et al. (2015), only option D was evaluated for the Ti centres, as it has been demonstrated to be the most reliable for

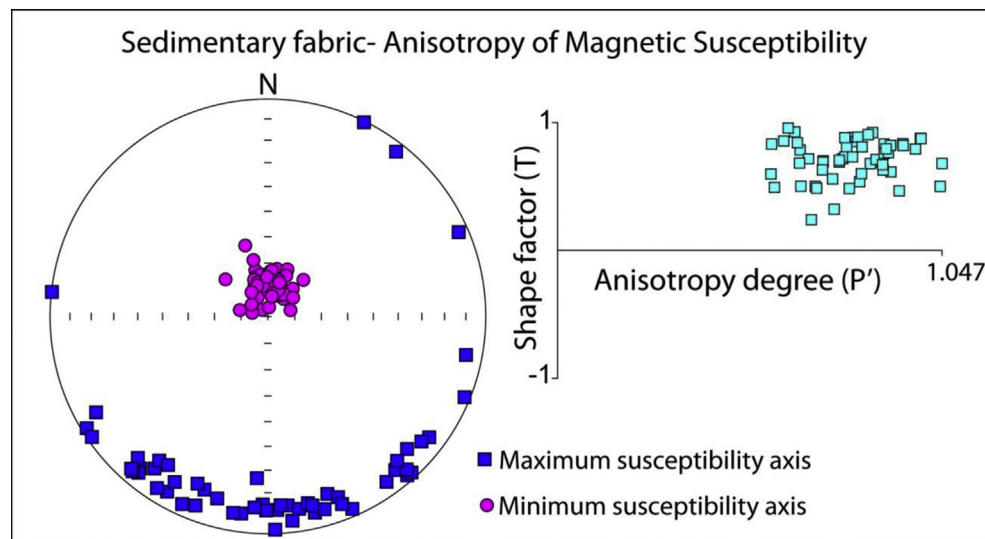


Fig. 3. Sedimentary fabric of the slackwater deposits (interior facies), in the lower part of TD1, as shown by the Anisotropy of Magnetic Susceptibility (AMS). Stereographic projection shows the distribution of the maximum (squares) and minimum (dots) susceptibility axes on to the lower hemisphere. Cartesian diagram on the right shows the shape of the magnetic ellipsoid (T) and the degree of anisotropy (P'). All samples display foliated magnetic anisotropy ($T > 0$) (see text for discussion), coherent with a depositional fabric on a slightly inclined surface.

Early Pleistocene deposits. Final Dose Response Curves (DRCs) were obtained by pooling all the repeated ESR intensities into a single graph as recommended by Duval (2012).

The equivalent dose (D_E) values were calculated with the Microcal Origin 8.5 software using the Levenberg-Marquardt algorithm by chi-square minimization. For the Al center, a single saturating exponential + linear function (SSE + LIN) was fitted through the experimental points, while the Ti-2 function was employed for the ESR signal of the Ti centers Duval et al. (2017).

New dose rate calculations were carried out using a combination of *in situ* and laboratory measurements. Gamma dose rate values were assessed on site with a NaI probe and evaluated using the Threshold approach as described in Duval and Arnold (2013). External alpha and beta dose rates were derived from U, Th and K concentrations obtained by ICP-MS analysis of ~5 g of powdered dry raw sediment. The dose rate conversion factors are from Guérin et al. (2011). Values were corrected with β and α attenuations for spherical grains (Brennan et al., 1991; Brennan, 2003; Guérin et al., 2012) and water attenuation formulae from Grün (1994). A water

content (dry weight) of 15 + 5% was assumed for all samples and an internal dose rate was assumed to be $50 \pm 30 \mu\text{Gy/a}$ based on the work from Vandenberghe et al. (2008) and assuming an α -efficiency k-value of 0.15 ± 0.10 (Yokoyama et al., 1985). The cosmic dose rate was calculated from the equations of Prescott and Hutton (1994), with latitude, altitude and depth corrections. ESR age calculation was performed using a non-commercial software based on DRAC (Durcan et al., 2015) which takes into account the uncertainties derived from concentrations, depth, water content, *in situ* gamma dose rate, attenuations and D_E values. The errors associated with total doses, equivalent doses and ESR age results are given at 1σ .

3.3. U-Pb geochronology

Two flowstones were sampled for U-Pb dating, including the top "stalagmitic crust" and a lower flowstone within the upper part of TD1 (Fig. 2). Prior to U-Pb isotope dilution analysis, reconnaissance U-Th-Pb concentration data were obtained by performing laser

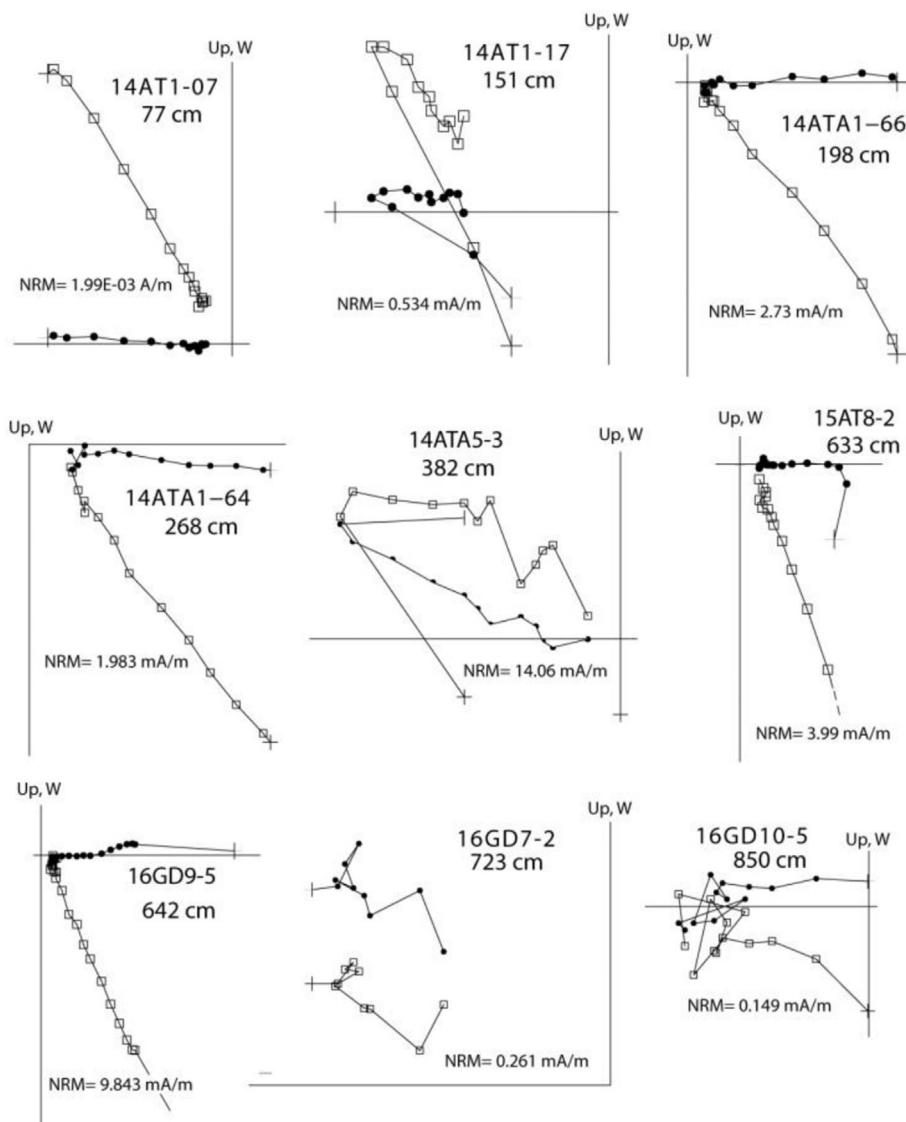


Fig. 4. Examples of progressive alternating field demagnetization displayed by vector end point diagrams (Zijderveld, 1967) of representative samples. Each data point represents the Natural Remanent Magnetization (NRM) end vector for individual demagnetization steps projected onto the horizontal (solid symbols) and vertical (open symbols) plane. Initial value of NRM (A/m) is also shown. Diagrams are shown in geographic coordinates.

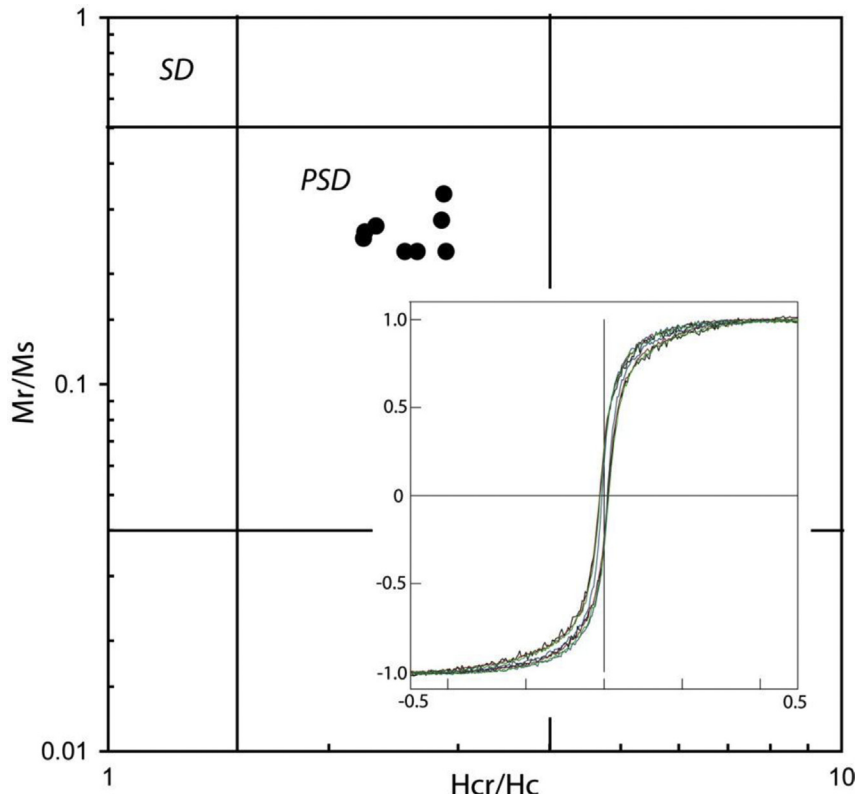


Fig. 5. Examples of representative hysteresis loops (inset) for the clayey siltstones and sandstones of the cave interior facies, and corresponding magnetic grain size on a Day diagram (Day et al., 1977). SD: Single Domain, PSD: Pseudo-single Domain. M_r : Saturation remanent magnetization, M_s : Saturation magnetization, H_{cr} : Coercivity of remanence, H_c : Coercivity.

ablation traverses perpendicular to the growth layers of each sample. As noted in Woodhead et al. (2012) this allows location of optimal layers for dating i.e those with high U/Pb ratio.

Analytical methods follow closely those published previously by Woodhead et al. (2006, 2012). Multiple aliquots of solid sample (not powders), typically weighing ~50 mg, are removed from the optimal layers in the speleothem sample identified by the laser ablation analysis, using a dental drill. The pieces of calcite removed in this way are placed into pre-cleaned disposable polyethylene cups and moved to a multiple-HEPA filtered clean room environment. Samples were briefly leached 2 times in very dilute (~0.01 M) three-times teflon distilled HCl, with each cycle lasting around a minute, and then repeatedly washed in ultra-pure water before being dried in a HEPA filtered laminar flow hood. This step is critical to the elimination of Pb contaminants resulting from sample handling which can easily dominate the Pb budget of the entire sample unless removed.

Individual samples were weighed into pre-cleaned teflon beakers and treated with sufficient 6N HCl to ensure complete dissolution. A mixed ^{233}U - ^{205}Pb tracer, calibrated against EarthTime (<http://www.earth-time.org>) reference solutions, was then weighed into the vials and each one sealed and refluxed on the hotplate for several hours to ensure complete sample-spike equilibration. Samples were then dried down and taken up in 0.6N HBr for Pb separation using AG 1X-8 anion exchange resin. The eluate was subsequently processed through the same column now filled with Eichrom TRU ion-specific resin, to separate U.

Isotope ratios were determined on a Nu Plasma MC-ICPMS using a DSN-100 desolvation unit and MicroMist glass nebuliser, operating in the range 50–100 $\mu\text{l}/\text{min}$ uptake. Instrumental mass bias effects were monitored and corrected using NIST SRM 981

reference material in the case of Pb, and the sample's internal $^{238}\text{U}/^{235}\text{U}$ ratio in the case of U. Instrument data files were processed initially using an in-house designed importer, operating within the Iolite environment (Paton et al., 2011), which considers all data and reference material analyses obtained throughout a particular analytical session and permits a variety of corrections for instrumental mass bias and drift. The resulting data, now corrected for instrumental effects, were then processed for isotope-dilution calculations and blank correction using the Schmitz and Schoene (2007) software.

4. Results

4.1. Paleomagnetism

As part of the sedimentary fabric study, the measurement of the AMS was carried out in the inclined laminar bedding silts and clays that appear in the lower part of the stratigraphic section. The distribution of the maximum axes of susceptibility show an overall tilt to the south and parallel to the measured dip of the laminae, whereas the minimum axes of susceptibility are normal to the lamination (Fig. 3). Axis distributions of this type are quite common in sedimentary rocks that have a primary inclination, providing further support for the origin of this cave interior facies. The anisotropy degree of 1.034 is consistent with clay-rich sediments as seen in a number of studies (see Tarling and Hrouda, 1993; Parés et al., 2007, 2010) and so is the shape of the ellipsoid as indicated by the T parameter (Fig. 3). Overall these observations are coherent with parallel accretion concordant to the dip of the underlying bedrock, and with the fluvial origin of this facies.

Demagnetization diagrams (Fig. 4) show generally well

behaved, stable remanent magnetization directions upon stepwise alternating field demagnetization. Many samples have a secondary low-coercivity component, possibly a viscous magnetization as the sediments have not been exhumed or thermally re-activated. Such low stability components are typically removed at fields of 15–20 mT and are apparent in samples where the high coercivity component has a negative inclination (e.g., 14AT.17, 14AT5-3 in Fig. 4). The orientation of this viscous component typically conforms to that of the present day field at the locality and hence has not been further considered in our study. Taken together the demagnetization of the NRM and hysteresis curves (Fig. 5) suggest that PSD magnetite is present in the studied silts and clays, in agreement with our previous studies of sediments from the same cave system (Parés et al., 2016) and with numerous cave deposits elsewhere (e.g., Bosak et al., 2003; Rossi et al., 2016). The magnetostratigraphy of the sampled interval (Fig. 6), expressed as the Virtual Geomagnetic Pole Latitude (VGP Lat) position (Table 1), reveals that, for the most part, the cave interior deposits display reverse polarity. Data from the lowermost cave interior sediments

are scarcer, due to the abundance of sandy silts that have produced either inconclusive or non interpretable demagnetization diagrams. A 100 cm-thick interval of normal polarity is observed at a depth between 2 and 3 m, and around a depth of 5.5 and 6.5 two shorter intervals of the same polarity as well (N3, N2, and N1 respectively, Fig. 6).

4.2. ESR dating

The fitting results derived from the Al centre (Fig. 7) show an excellent goodness-of-fit for sample TD1-08-01bis (adjusted $r^2 > 0.99$) resulting in a relative D_E error of 9%. In comparison, TD1-08-01 and TD1-08-02 show instead a regular goodness-of-fit (adj. $r^2 < 0.97$), resulting in somewhat higher relative D_E errors of 22%. In contrast, no reliable ESR data have been obtained from the Ti centres (Option D) in two of the three samples analysed in this work. The low intensity of the signals makes them quite difficult to measure, with noisy spectra resulting in scattered Dose Response Curves (DRC), unsatisfactory goodness-of-fit (adj. $r^2 < 0.85$), and

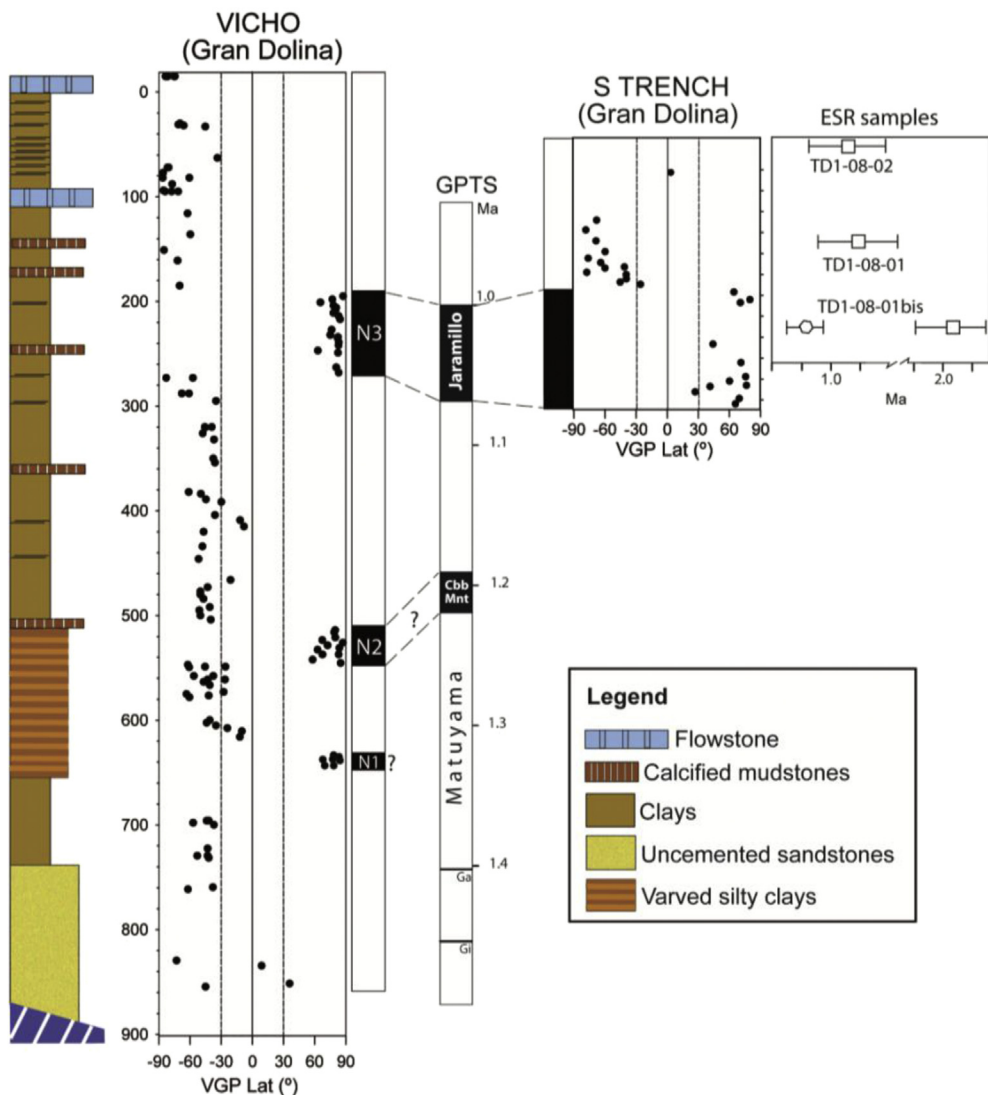


Fig. 6. Virtual Geomagnetic Pole (VGP) latitude positions for both Vicho (left) and South Trench (right) sections. Each dot corresponds to the VGP latitude of a specimen. GPTS (Geomagnetic Polarity Time Scale) shows the Jaramillo Subchron (1.00–1.07 Ma), and three additional, shorter normal polarity intervals within Matuyama: Cobb Mountain (1.19–1.122 Ma), Gardar (Ga, 1.4 Ma) and Gilsa (Gi, 1.5 Ma) (Singer, 2014). Also shown is the location of samples for ESR analysis. Squares (polygon) show Al (Ti) data (see main text for discussion).

Table 1

Paleomagnetic data. Dec & Inc = Declination and Inclination of the Characteristic Remanent Magnetization (ChRM) direction; MAD = Maximum angular deviation; VGP LAT = latitude of the Virtual Geomagnetic Pole Position.

VICO Section					
Specimen	Depth (cm)	Dec	Inc	MAD	VGP Lat
14AT1.05.B	-15.0	176.4	-55.7	6.1	-83
14AT1.01.A	-15.0	164.2	-53.8	4.5	-75
14AT1.02.A	-15.0	174.7	-54.4	12.3	-82
14AT1.03.A	-15.0	189.5	-48.1	7.0	-75
14AT1.05.A	-15.0	185.6	-65.4	18.9	-84
14ATA1-70	30.0	182.7	-39.2	42.6	-70
14ATA1-71	31.0	205.9	-63.2	12.2	-71
14ATA1-72	32.0	192.7	-37.4	32.8	-66
14ATA1-73	33.0	200.6	-3.0	11.3	-45
14AT1.06	63.0	239.4	-30.8	16.8	-34
14AT1.10.A	72.0	192.8	-61.3	2.1	-81
14AT1.10.B	72.0	189.8	-65.0	16.9	-82
14AT1.07	77.0	184.1	-59.0	1.9	-86
14AT1.09.A	82.0	180.9	-64.2	8.9	-86
14AT1.09.B	82.0	206.9	-40.8	38.5	-61
14AT1.12.B	88.0	173.5	-70.3	25.6	-77
14AT1.12.A	94.0	183.9	-58.4	2.1	-86
14AT1.11.A	95.0	185.5	-50.1	9.2	-78
14AT1.11.C	95.0	202.2	-54.7	14.0	-71
14AT1.11.B	95.0	183.4	-56.3	10.5	-84
14AT1.14	116.0	164.4	-79.0	35.6	-62
14AT1.16.A	136.0	206.6	-38.6	31.3	-60
14AT1.17	151.0	184.0	-57.8	8.9	-85
14AT1.18	161.0	185.9	-43.0	33.5	-72
14AT1.20.B	185.0	180.0	-30.0	15.5	-70
14ATA1-65	195.0	3.0	62.1	5.4	88
14ATA1-66	198.0	351.8	50.6	10.1	77
14ATA1-67	201.0	329.2	56.4	14.9	66
14ATA1-68	204.0	9.1	52.7	10.4	78
14ATA1-69	206.0	359.1	52.7	9.2	81
14ATA1-48	208.0	12.0	58.4	8.6	80
14ATA1-49	211.0	353.9	69.6	14.2	78
14ATA1-50	214.0	356.6	66.2	6.7	83
14ATA1-51	217.0	354.5	58.3	7.3	85
14ATA1-53	227.0	341.7	63.3	7.8	77
14ATA1-47	232.0	345.8	52.3	8.2	75
14ATA1-54	234.0	5.9	66.1	7.9	83
14ATA1-55	235.0	350.9	58.5	13.4	82
14ATA1-56	239.0	8.4	59.6	9.7	83
14ATA1-58	247.0	28.7	75.9	12.3	63
14ATA1-59	249.0	357.7	54.6	10.0	83
14ATA1-62	242.0	8.0	58.5	3.6	83
14ATA1-63	263.0	356.9	68.0	7.1	81
14ATA1-64	268.0	1.9	55.3	7.2	83
14AT1.31.A	273.0	190.8	-21.1	24.4	-57
14AT1.32	273.0	171.2	-59.3	21.2	-83
14AT1.33.A	288.0	177.5	-36.5	9.8	-68
14AT1.34.A	288.0	161.3	-33.1	25.0	-61
14AT1.36	295.0	137.8	-4.2	3.1	-35
14AT1.39	320.0	165.4	-0.1	14.2	-46
14AT1.40	320.0	140.0	-11.2	4.8	-39
14AT1.42	326.0	171.3	-1.7	8.4	-48
14AT1.44	332.0	206.9	9.5	6.6	-37
14ATA5-1	350.0	220.6	-8.3	17.0	-38
14ATA5-2	354.0	212.1	6.4	15.7	-36
14ATA5-3	382.0	201.0	-35.6	18.2	-61
14ATA5-4	383.7	209.5	-21.4	12.8	-50
14ATA5-6	389.0	187.1	4.8	19.9	-45
14ATA5-7	391.6	209.8	21.8	11.1	-30
14ATA5-10	404.0	206.0	12.2	19.2	-36
14ATA5-11	409.0	230.7	36.5	20.0	-12
14ATA5-13	415.0	239.7	33.6	16.8	-8
14ATA5-14	420.0	139.0	-31.4	6.0	-47
14ATA5-15	434.0	150.0	-18.7	10.4	-48
14ATA5-17	446.0	142.4	-37.0	20.8	-52
16GD6.13	466.0	211.0	36.0	6.0	-21.0
16GD6.11	473.0	207.0	-3.0	10.0	-43.0
16GD6.10	477.0	178.0	-4.0	4.0	-50.0
16GD6.9	480.0	174.0	-4.0	1.0	-50.0
16GD6.8	484.0	182.0	0.0	6.0	-47.0
16GD6.6	492.0	167.0	10.0	11.0	-41.0

(continued on next page)

Table 1 (continued)

VICO Section					
Specimen	Depth (cm)	Dec	Inc	MAD	VGP Lat
16GD6.5	495.0	173.0	-7.0	7.0	-51.0
16GD6.4	500.0	182.0	-5.0	5.0	-50.0
16GD6.3	504.0	186.0	15.0	3.0	-40.0
16GD6.2	514.0	1.0	52.0	2.0	80.0
16GD6.1	516.0	5.0	52.0	3	79.0
15AT8-1	516.0	344.0	59.0	7.0	78
15AT8-2	520.0	1.0	69.7	7.6	79
15AT8-3	521.0	13.0	62.4	10.4	80
15AT8-29	524.0	329.0	66.0	9.0	68
15AT8-4	526.0	1.9	63.2	9.3	87
15AT8-5	529.0	22.7	67.0	6.0	73
15AT8-30	531.0	352.0	63.0	6.0	84
15AT8-6	533.0	14.5	78.8	21.2	63
15AT8-7	533.0	6.1	58.5	19.2	84
15AT8-8	537.0	327.3	74.6	19.4	83
15AT8-11	537.0	28.9	57.6	15.1	68
15AT8-14	542.0	336.0	80.8	19.5	58
15AT8-15	545.0	359.2	65.2	17.9	85
15AT8-56	547.0	194.0	-32.0	4.4	-62
15AT8-16	549.0	184.5	38.5	8.5	-25.8
15AT8-36	549.0	165.0	0.1	5.0	-45.5
15AT8-58	549.0	176.0	-25.0	6.0	-60.8
15AT8-39	558.0	203.0	11.0	32.0	-37.6
15AT8-60	558.0	190.8	-19.5	10.0	-56.3
15AT8-21	561.0	175.0	38.0	23.8	-26.2
15AT8-61	561.0	215.7	-14.6	8.0	-43.0
15AT8-41	563.0	200.0	-7.0	22.0	-46.9
15AT8-42	566.0	191.0	10.0	27.0	-41.0
15AT8-46	573.0	205.0	29.0	27.0	-27.6
15AT8-47	575.0	161.0	-38.0	27.0	-63.5
15AT8-28	577.0	154.2	-0.1	7.7	-42.0
15AT8-95	578.0	181.0	-25.0	7.0	-60.6
16GD8-13	600.0	163.0	8.0	13.0	-41.0
16GD8-12	602.0	159.0	0.0	12.0	-44.0
16GD8-11	605.0	164.0	21.0	9.0	-35.0
16GD8-10	608.0	150.0	33.0	15.0	-24.0
16GD8-9	611.0	147.0	51.0	8.0	-10.0
16GD8-7	616.0	181.0	55.0	30.0	-12.0
15AT7-12	632.0	356.0	52.0	4.0	80.0
16GD8-2	633.0	3.0	57.0	2.0	85.0
16GD8-1	636.0	16.0	59.0	5.0	78.0
15AT7-13	636.0	7.0	39.0	6.0	69.0
16GD9-3	636.0	12.0	64.0	3.0	81.0
16GD7-14	638.0	5.0	62.0	3.0	86.0
16GD9-5	642.0	349.0	66.0	2.0	80.0
15AT7-16	642.0	23.0	64.0	5.0	73.0
16GD7-13	642.0	353.0	40.0	6.0	70.0
16GD7-9	696.0	236.0	-44.0	6.0	-42.0
16GD7-8	696.0	233.0	-45.0	15.0	-44.0
16GD7-7	698.0	193.0	-22.0	9.0	-57.0
16GD7-6	700.0	212.0	3.0	13.0	-37.0
16GD7-2	723.0	218.0	-19.0	6.0	-43.0
16GD7-1	730.0	203.0	-22.0	10.0	-53.0
16GD10-25	732.0	222.0	-22.0	7.0	-42.0
16GD10-20	762.0	202.0	-38.0	10.0	-62.0
16GD10-19	760.0	219.0	-8.0	6.0	-38.0
16GD10-10	835.0	325.0	-51.0	6.0	9.0
16GD10-9	830.0	166.0	-49.0	8.0	-73.0
16GD10-8	852.0	300.0	37.0	16.0	36.0
16GD10-4	855.0	213.0	-16.0	3.0	-45.0
S TRENCH Section					
Specimen	Depth (cm)	Dec	Inc	MAD	VGP Lat
TD1-13-064	0.0	294.0	-34.0	8.0	4.2
TD1-13-056	44.0	177.0	-35.0	10.0	-67.2
TD1-13-054	53.0	176.0	-49.0	5.5	-77.5
TD1-13-052	63.0	176.0	-36.0	6.3	-67.7
TD1-13-050	73.0	221.0	-58.0	7.0	-58.9
TD1-13-048	79.0	199.0	-66.0	3.2	-75.2
TD1-13-046	83.0	217.0	-69.0	4.5	-63.1
TD1-13-044	87.0	248.0	-60.0	6.9	-40.4
TD1-13-042	88.0	222.0	-61.0	3.2	-59.1
TD1-13-040	92.0	197.0	-66.0	3.8	-76.5

Table 1 (continued)

S TRENCH Section						
Specimen	Depth (cm)	Dec	Inc	MAD	VGP Lat	
TD1-13-038	94.0	235.0	−35.0	4.6	−38.6	
TD1-13-036	98.0	230.0	−26.0	8.9	−38.5	
TD1-13-034	101.0	222.0	−27.0	6.0	−44.5	
TD1-13-032	103.0	238.0	−5.0	7.3	−25.0	
TD1-13-030	108.0	7.0	27.0	12.0	61.6	
TD1-13-026	118.0	352.0	59.0	5.1	83.6	
TD1-13-022	122.0	340.0	50.0	23.8	70.5	
TD1-13-018	158.0	305.0	49.0	9.6	44.7	
TD1-13-016	175.0	340.0	52.0	2.6	71.6	
TD1-13-014	188.0	343.0	57.0	5.2	76.2	
TD1-13-013	192.0	331.0	43.0	4.1	60.7	
TD1-13-012	196.0	16.0	57.0	3.8	77.0	
TD1-13-010	197.0	58.0	48.0	4.2	42.0	
TD1-13-008	202.0	334.0	−29.0	9.1	27.7	
TD1-13-003	208.0	360.0	39.0	5.1	70.0	
TD1-13-005	213.0	26.0	50.0	8.0	66.4	

thus meaningless D_E results. However, sample TD1-08-01bis shows a somewhat less scattered DRC, from which D_E has been obtained (Fig. 7). Fitting results with equal weights and data weighted by the inverse of the squared errors provided D_E values of 1387 ± 249 and 1141 ± 181 Gy, respectively. These values differ by about 21%, which is most likely due to the scatter in the experimental data points. Consequently, we consider the mean D_E value 1264 ± 174 Gy as being the best estimate for the burial dose of this sample.

Calculations provide ESR-Al age results of 1.12 ± 0.25 , 1.20 ± 0.27 and 2.27 ± 0.22 Ma for samples TD1-08-02, TD1-08-01 and TD1-08-01bis, respectively. Overall, these results are apparently coherent with both the chronostratigraphic framework and previous numerical ages (Moreno et al., 2015) suggesting an Early Pleistocene chronology for TD1. For example, the new age of TD1-08-01 is very similar to that previously obtained by Moreno et al. (2015) (−3%) while it is higher by +41% for sample TD1-08-02. This is mostly because previous age calculations by Moreno et al. (2015) were performed using the same gamma dose rate value as for TD1-08-01. The new *in situ* measurements and the radioelement concentrations obtained by ICP-MS instead reveal that the gamma dose rate at TD1-08-02 site was lower by 35%. Finally, sample TD1-08-01bis yields an age that is more than two times older than those previously obtained by Moreno et al. (2015) (2.3 Ma vs. 0.9 Ma). This difference is mostly due to the D_E values derived from each study (3403 ± 310 vs 1631 ± 332 , respectively), although a more limited impact due to a somewhat smaller total dose rate cannot be discounted.

As far as sample TD1-08-01bis, two factors could possibly explain a bias in age. A water content of $15 \pm 5\%$ (1σ) was first assumed for the age calculation, in order to cover a wide range of values (5–25%), including the current water content at a 2 sigma confidence level. A slight increase of the water content to 20% instead would result in a moderate age increase to 0.90 ± 0.13 Ma. Moreover, the reliability of the fitting results may be questioned as one may observe that the natural point is actually much lower than any other points in the DRC. This has most likely the effect of decreasing the D_E value and thus the age. To evaluate this impact, we calculated the D_E without taking into account the natural point, obtaining a D_E of 1892 ± 447 (data weighted by the inverse of the squared experimental errors, i.e., $1/s^2$) and 2087 ± 646 (equal weights). Considering the resulting mean D_E value 1990 ± 137 Gy, the resulting ESR-Ti age obtained becomes significantly older (1.33 ± 0.10 Ma), which may be considered as the maximum possible age for the sample. Consequently, it is probable that the true age of TD1-08-01bis is somewhat higher than the 0.84 ± 0.12 , although this cannot be exactly quantified.

The new results show an excellent goodness-of-fit ($r^2 > 0.99$), which contrast with the previous data ($r^2 < 0.98$) from Moreno et al. (2015), resulting in a more reliable dose estimate and thus a more accurate age result. However, this ESR-Al age is far older than those obtained for TD1-08-01 and TD1-08-02. This may actually reflect some vertical variations of the sedimentary fluvial environment within the top of TD1 unit. The three ESR samples were indeed collected from two different facies observed within TD1, as defined by Campaña et al. (2017). TD1-08-01bis may be correlated to facies B, comprised of laminated cemented clayey silt, while TD1-08-01 and TD1-08-02 were collected from facies A, a laminated sandy silt with soft nodules. The change from facies B to facies A indicates an increase in the flow energy and the sorting of larger particles (Campaña et al., 2017) (Fig. 2). Therefore, these two sedimentary facies suggest different transport and depositional conditions, and thus bleaching histories for the three samples. The higher energy environment of facies A may indicate a more effective zeroing of the Al-centre for samples TD1-08-01 and TD1-08-02, in comparison with TD1-08-01bis.

In comparison, the Ti-Li signal measured in TD1-08-01bis gives a significantly younger age result of 0.84 ± 0.12 Ma. Based on the principle of the MC approach, such a difference between ESR-Al and ESR-Ti ages for this sample may be interpreted as an incomplete bleaching of the Al signal during transportation, which is consistent with previous observations made on the sedimentary environment. Consequently, we consider the Ti result as the most reliable estimate for the burial age of sample TD1-08-01bis (see Table 2).

4.3. U-Pb Geochronology

The reconnaissance laser ablation data reveal typically low, and relatively constant, uranium concentrations around 50 ppb but with very large variations in Pb concentration from low ppb to high ppm values (Fig. 8). Although areas with the highest U/Pb ratios (identified for analysis using laser ablation techniques) were sampled for the subsequent solution isotope dilution analyses, the U-Pb data reveal no discernible radiogenic ingrowth with increasing U/Pb ratios – at least within analytical uncertainties (see Table 3). As a result no U-Pb age information could be obtained for the two flowstones. At the present time therefore these materials remain undatable with traditional U-Pb isotope dilution methods. Research is however continuing into the development of *in situ* (laser ablation) dating methodologies which might ultimately allow the isolation of more radiogenic horizons suitable for age determination.

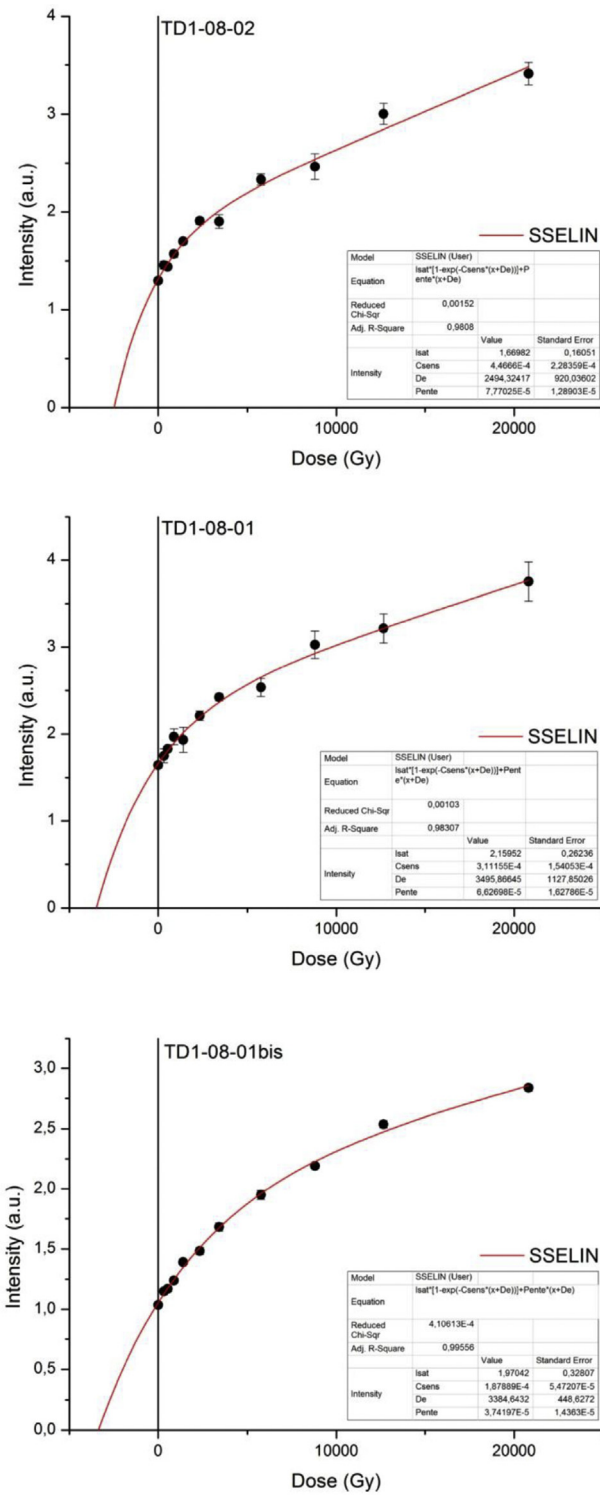


Fig. 7. ESR dose response curves (DRC) of the Al and Ti-Li (option D) signals measured in three quartz samples from the TD1 level in Gran Dolina site. For each sample, final D_e values were derived the pooled ESR intensities, as recommended by Duval (2012).

5. Discussion

The magnetostratigraphic study of the lowermost part of the sequence at Gran Dolina (Vicho section) has led to the unambiguous identification of three normal magnetozones (N3, N2 and N1 from bottom to top) within deposits mostly dominated by a reverse

polarity (Fig. 6). In comparison, only one normal and one reverse magnetozone were identified in the shorter Southern trench where ESR samples were collected. A tight litho- and magnetostratigraphic correlation is nevertheless possible for those two sections that are distant by a few meters only, positioning the Southern trench deposits in the top part of the Vicho profile.

The presence of the Matuyama-Brunhes boundary (MBB) near the TD7-TD8 boundary has been reported at about 10 m above the youngest cave interior facies horizon (Parés et al., 2013 for discussion), and recent luminescence dates from TD6 sediments, right below the MBB, produced a weighted mean age of 846 ± 57 ka (Arnold et al., 2014), which can be taken as a *post quem* for the cave interior sediments. On the other hand, our new ESR results reveal ages of 1.12 ± 0.25 (TD1-08-02) and 1.20 ± 0.27 (TD1-08-01) for the reverse magnetozone located at the top of unit TD1 and above magnetozone N3 (Fig. 6). These two ages are derived from the measurement of the Al centre, which means that they should be considered as maximum possible age estimates for the deposits dated. In other words, the true age of those deposits is either similar or younger than the ESR-Al ages obtained. The chronology of the top part of TD1 is thus constrained between the MBB and the weighted mean Al age of 1.16 ± 0.18 Ma derived from the two ESR samples.

Consequently, both the MBB above TD1 and the ESR ages strongly suggest that normal chron N3 of the local magnetostratigraphy corresponds to the Jaramillo Subchron (C1r1n; 1.00–1.07 Ma). The ESR sample TD1-08-01bis collected within N3 provides an ESR-Al age of 2.27 ± 0.2 Ma and an ESR-Ti age 0.84 ± 12 Ma. While the former should be interpreted as a maximum age, the latter instead may be considered as the best age estimate for the deposits and, as discussed in the previous section, by considering a more realistic water content of 20% the age increases to 0.90 ± 0.13 Ma, consistent within error with a Jaramillo chronology.

There are two older short normal polarity intervals in the section, namely N1 and N2, much shorter and hence difficult to interpret. On the GPTS two short-lived normal polarity intervals can be observed below Jaramillo, namely Cobb Mountain (1.19–1.22 Ma) and Bjorn (1.25 Ma) (Singer, 2014), which we can tentatively correlate to polarity intervals N2 and N1 respectively. We are aware that assigning interval N2 to Cobb Mountain implies a reduction of accumulation rate downwards between depths 5 to 2.5 m, but given the nature and accumulation history of cave deposits it is a reasonable hypothesis. The appearance of well laminated, varved sediments at depths 4.8–6.2 m suggests a variable sediment accumulation rate in the section. Hence, because (1) accumulation rates can be rather variable, and (2) there is a number of short-lived, ephemeral normal polarity intervals between 1.7 Ma (top Olduvai) and 1.0 Ma (bottom Jaramillo) (Gradstein et al., 2012), the assignation of intervals N1 and N2 remains at this stage somewhat ambiguous, whereas Jaramillo seems to be rather well documented in the section. In any case the interpretation of N1 does not affect the inference that sedimentation in the cave started within the Matuyama Chron, before Jaramillo, and most likely before the Cobb Mountain normal short interval.

Our new paleomagnetic record of the cave interior sediments (TD1) at the base of the Gran Dolina section adds an important constraint on the overlying stone tool-bearing level TD4. Sedimentary unit TD4 predates both a luminescence age of 850 ka, and the Matuyama-Brunhes boundary (0.78 Ma), and it is younger than the cave interior sediments that recorded the Jaramillo Subchron. These chronological constraints are consistent with the biostratigraphical evidence. Significant microfaunal taxa suggest that level TD4 of Gran Dolina is younger than the lower red units of Sima del Elefante (Cuenca-Bescós et al., 2015), with an estimated burial age of 1.2 ± 0.16 Ma (Carbonell et al., 2008). They indicate that

Table 2

ESR ages and associated data obtained (Bl = bleaching percentage, expressed as the relative difference between the ESR intensities of the natural and bleached aliquots); D_{cos} = cosmic dose rate; Dint = internal dose rate; Da = total dose rate; DE = equivalent dose).

This study										Moreno et al. (2015)	
Sample	Centre	Bl (%)	D_α ($\mu\text{Gy/a}$)	D_β ($\mu\text{Gy/a}$)	D_γ ($\mu\text{Gy/a}$)	D_{cos} ($\mu\text{Gy/a}$)	D_{int} ($\mu\text{Gy/a}$)	D_a ($\mu\text{Gy/a}$)	D_E (Gy)	Age (Ma)	Age (Ma)
TD1-08-02	AI	50.6 ± 0.8	44 ± 10	1347 ± 22	639 ± 38	30 ± 3	50 ± 30	2110 ± 54	2374 ± 517	1.12 ± 0.25	0.79 ± 0.06
TD1-08-01	AI	65.7 ± 0.3	65 ± 15	1774 ± 29	1087 ± 63	28 ± 3	50 ± 30	3004 ± 63	3609 ± 798	1.20 ± 0.27	1.25 ± 0.13
TD1-08-01bis	AI	52.4 ± 1.4	31 ± 7	759 ± 13	632 ± 38	27 ± 3	50 ± 30	1499 ± 51	3403 ± 310	2.27 ± 0.22	0.92 ± 0.19
	Ti-Li (option D)									1264 ± 174 ka	0.84 ± 0.12 -

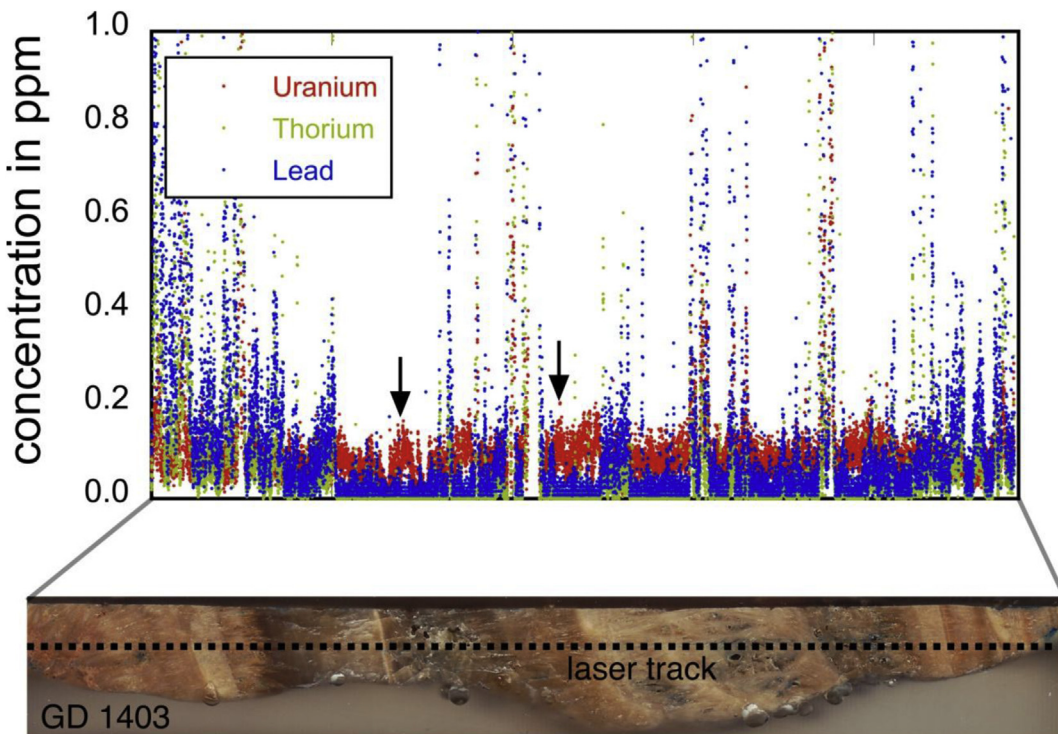


Fig. 8. Laser ablation traverses perpendicular to the growth layers of each sample for reconnaissance of U-Th-Pb concentration data.

Table 3

Uranium and lead isotopic compositions of Gran Dolina TD1 speleothem samples analysed by MC-ICP-MS at the University of Melbourne.

Speleothem	Sample	U (ppm)	Pb (ppm)	$^{238}\text{U}/^{206}\text{Pb}$	% err	$^{207}\text{Pb}/^{206}\text{Pb}$	% err	$^{204}\text{Pb}/^{206}\text{Pb}$	% err	corr. coeff.
TD2-1	1	0.054	0.009	21.142	1.03	0.82879	0.14	0.05279	0.25	-0.76
	2	0.076	0.012	21.094	0.98	0.82855	0.14	0.05262	0.25	-0.75
	3	0.053	0.008	21.865	1.30	0.82760	0.16	0.05242	0.48	-0.82
	4	0.074	0.010	26.893	1.53	0.82797	0.18	0.05287	0.29	-0.85
	5	0.055	0.010	19.766	1.43	0.82849	0.17	0.05262	0.28	-0.80
	6	0.083	0.015	19.550	0.86	0.82921	0.12	0.05387	0.22	-0.77
GD1403	1	0.049	0.008	21.854	1.37	0.81825	0.18	0.05170	0.50	-0.87
	2	0.067	0.009	24.717	53.69	0.84113	12.59	0.04448	0.50	-0.01
	3	0.046	0.012	13.298	0.81	0.82039	0.13	0.05215	0.23	-0.72
	4	0.066	0.004	65.613	3.49	0.82185	0.39	0.05234	0.51	-0.97
	5	0.053	0.010	18.077	1.05	0.82760	0.15	0.05242	0.58	-0.73
	6	0.068	0.005	50.475	1.50	0.82182	0.19	0.05197	0.34	-0.87

TD4 level, which postdates the cave interior sediments, is younger than the Sima Elefante red units (TELRU of Cuenca-Bescós et al., 1999, 2015) fauna.

From a karst evolution point of view, the “stalagmitic crust” at the top of TD1 marks an important step in the Gran Dolina sedimentary infilling history and by inference in the middle tier of the karst. Below such a flowstone sediments are slackwater deposits,

whereas on top the sedimentary record shows an abundance of coarse deposits, gravels and sandstones of allochthonous origin for the most part. Such a pronounced change, likely related to an environmental shift that occurred between ca 1.0 and 0.9 Ma (MIS 25?), reflects the development of a cave entrance that allowed the beginning of the allochthonous sediment accumulation in the cavity, and a significant drop of the water table. Although some thin

flowstones are found in younger units (e.g., TD7-TD8), the cavity remains essentially above the phreatic level until it is completely filled up by sediments (unit TD11). The time gap between the development of the basal stalagmitic crust and the first entrance of allochthonous deposits of unit TD4 remains to be determined and will inevitably slightly rejuvenate the age of this geo-unit.

From a broader geological perspective, this geochronological context also helps us to better understand the development and karst evolution of the Atapuerca system. Gran Dolina is one of several caves in the middle level tier of the karst. The middle karst level tier consists of a sub-horizontal passage located at

1000–1005 m a.s.l. (above sea level) in Cueva Mayor (Ortega et al. 2013, 2014). Along both Galería Baja and Galería del Silo (interior of Cueva Mayor) a unit of sandy clays and silts of unknown total thickness is blanketing the floor of the passages. The visible thickness, in prehistoric silos, is about 150 cm, but the contact with the limestone floor is not exposed. A thin flowstone is capping the clastic sediments in both passages. The magnetostratigraphic sections in these two conduits show similar trends: sediments at the bottom have reverse magnetization directions whereas at the top they have normal polarity. The remains of *Ursus deningeri* in the upper sediments suggests a Middle Pleistocene age (e.g., García

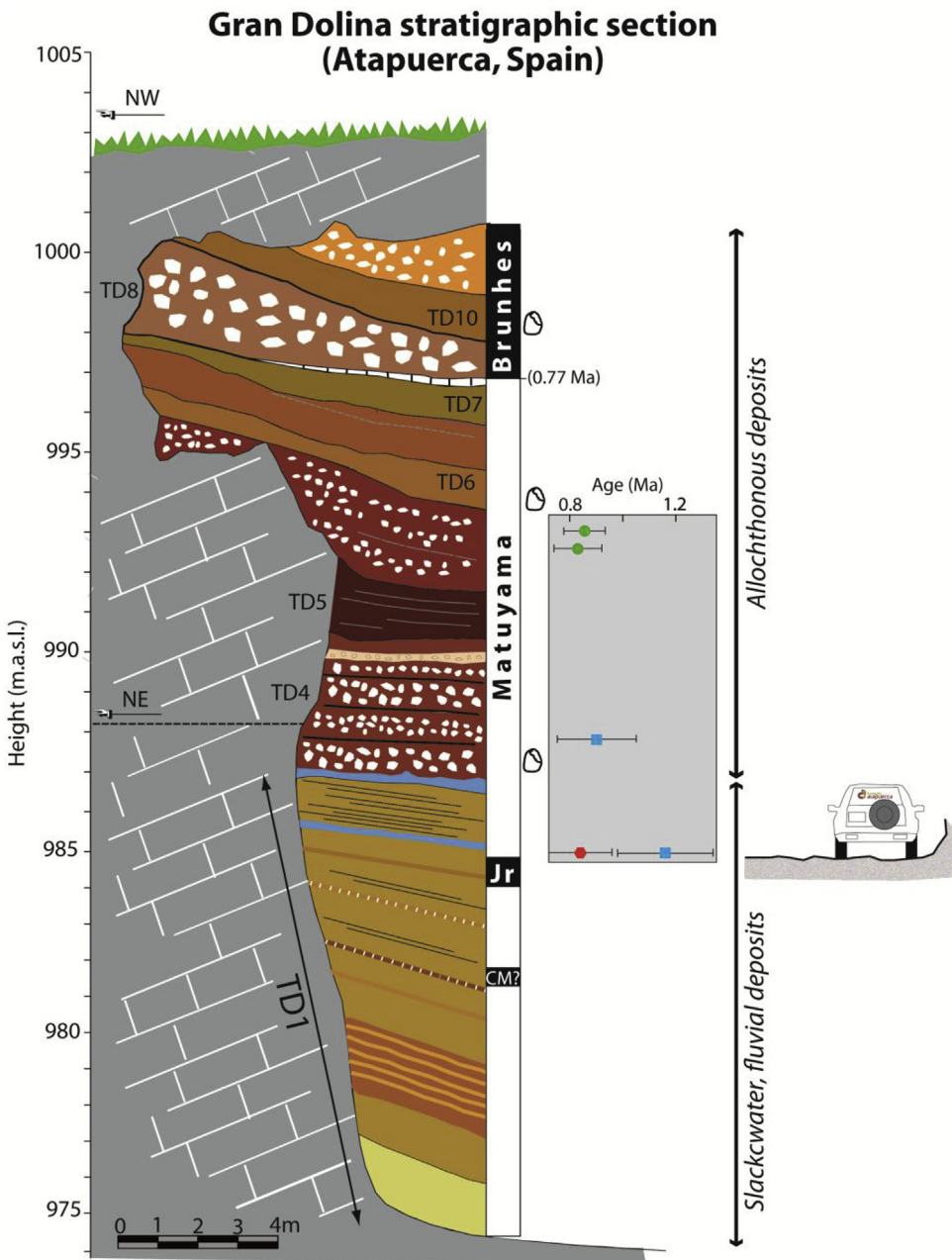


Fig. 9. Sedimentary infill at Gran Dolina site with magnetostratigraphic, OSL, and ESR results. Main lithostratigraphic units adapted from Campaña et al. (2016) and our own field observations. Notice the two main groups of sedimentary facies, including entrance (or allochthonous) facies deposits (TD4 through TD10) at the top, and slackwater, fluvial deposits (TD1) at the bottom, directly overlying the bedrock. In blue are shown the speleothems developed at the bottom unit TD1. Numerical ages include OSL (green) (Arnold et al. (2014), ESR-Al (blue), ESR-Ti (red) (Moreno et al., 2015 and this study). (For interpretation of the references to colour in this figure legend, the reader is referred to the Web version of this article.)

et al., 1997) and accordingly the R→N polarity change has been interpreted as the Matuyama-Brunhes boundary (Parés et al., 2013). The thickness of sediment underneath the sampled section is unknown, and therefore the polarity reversal age is only a minimum age for the cave formation. This is consistent with previous observations in Sima del Elefante (Middle level tier exposed along the railway trench, see Fig. 1), where the lowermost deposits (TE9) have a burial age of 1.22 ± 0.16 Ma (Carbonell et al., 2008). In the upper part of the Elefante section the Matuyama-Brunhes reversal has been described (Parés et al., 2007) and recent luminescence dates confirm such a polarity reversal (Arnold et al., 2014). In summary, current evidence suggests that the middle level tier in the Atapuerca karst system formed well before the Matuyama-Brunhes boundary as suggested by both paleomagnetism and terrestrial cosmogenic burial ages. The cave interior sediments at Gran Dolina targeted in the current study are flooring the middle level tier and have reverse polarity, which is consistent with the previous data, and shows that this level tier formed during in Matuyama times and before the Jaramillo Subchron according to our new data.

6. Conclusions

The archaeological layers at Gran Dolina, including artifact-bearing level TD4, are preceded by about 9 m of sterile, interior fluvial facies cave sediments that were deposited before the appearance of large openings to the cave (Fig. 9). The cave interior sediments are capped by a flowstone and followed by a pile of 15 m of exterior facies sediments (talus, slope, sliding bed deposits), where fossil and artifact-bearing horizons are found. The magnetic stratigraphy of the cave interior sediments reveals a dominant reverse magnetic polarity, coherent with a Matuyama age, and interrupted by a ca. 100 cm normal polarity magnetozone. Re-measured ESR ages on quartz grains in the upper part of TD1 produced an age range between 0.8 and 1.2 Ma, and therefore we interpret the normal magnetozone N3 as the Jaramillo Subchron (1.00–1.07 Ma). The oldest archaeological unit at Gran Dolina and artifact-bearing layer TD4 is overlying the studied layer TD1 and therefore post-dates the Jaramillo Subchron.

The flowstone between units TD1 and TD4 ("stalagmitic crust") indicate the proximity of the cavity to the vadose zone, and its formation shows a major change from interior facies (phreatic-vadose zone) to eventual cave entrances development, an environmental change that allowed the accumulation of slope, talus, and debris cones that contain the fossil and artifact horizons that make the Gran Dolina site so special. Ongoing research on the flowstone that precedes such deposits will help in further constraining the age of such major paleoenvironmental change in the karst evolution and development at Atapuerca.

Acknowledgements

Access and permission to collect samples in Atapuerca was granted by Junta de Castilla y León. The authors are deeply indebted to the Atapuerca Research Team (EIA) and the Fundación Atapuerca for continuous support of this research. We are thankful to Miguel Ángel Martín for preparing field photographs (Fig. 2). Financial support for this work was obtained from Junta de Castilla y León and from MINECO Grants CGL2010-16821 and CGL2015-65387-C3-3-P. M. Duval's research is currently funded by an Australian Research Council Future Fellowship (FT150100215). U-Pb dating at Melbourne was conducted with funding from the Australian Research Council. MJS was funded by the Netherlands Organisation for Scientific Research grants NWO-ALW 823.01.003. We thank the three anonymous reviewers for their helpful constructive

comments and suggestions.

References

- Arnold, L.J., Demuro, M., Parés, J.M., Pérez-González, A., Arsuaga, J.L., Bermúdez de Castro, J.M., Carbonell, E., 2014. Evaluating the suitability of extended-range luminescence dating techniques over early and Middle Pleistocene time-scales: published datasets and case studies from Atapuerca, Spain. *Quat. Int.* <https://doi.org/10.1016/j.quaint.2014.08.010>.
- Balsley, J.R., Buddington, A.F., 1960. Magnetic susceptibility anisotropy and fabric of some Adirondack granites and orthogneisses. *Am. J. Sci.* **258A**, 6–20.
- Benito-Calvo, A., Pérez-González, A., 2015. Geomorphology of the Sierra de Atapuerca and the Middle Arlanzón Valley (Burgos, Spain). *J. Maps* **11**, 535–544.
- Bermúdez de Castro, J.M., Arsuaga, J.L., Carbonell, E., Rosas, A., Martínez, I., Mosquera, M., 1997. A hominid from the lower Pleistocene of Atapuerca, Spain: possible ancestor to Neandertals and modern humans. *Science* **276**, 1392–1395.
- Bermúdez de Castro, J.M., Pérez-González, A., Martín-Torres, M., Gómez-Robles, A., Rosell, J., Prado, L., Sarmiento, S., Carbonell, E., 2008. A new early Pleistocene hominin mandible from Atapuerca-TD6, Spain. *J. Hum. Evol.* **55**, 729–735.
- Bosak, P., Pruner, P., Kadlec, J., 2003. Magnetostratigraphy of cave sediments: application and limits. *Studia Geophys. Geod.* **47**, 301–330.
- Bosch, R.F., White, W.B., 2004. Lithofacies and transport of clastic sediments in karstic aquifers. In: Sasowsky, I.D., Mylroie, J.E. (Eds.), *Studies of Cave Sediments*. Kluwer Academic/Plenum Publishers, New York, pp. 1–22.
- Brennan, B.J., 2003. Beta doses to spherical grains. *Radiat. Meas.* **37** (4–5), 299–303.
- Brennan, B.J., Lyons, R.G., Philips, S.W., 1991. Attenuation of alpha particle track dose for spherical grains. *Int. J. Rad. Appl. Instrum. Part D. Nucl. Tracks Radiat. Meas.* **18**, 249–253.
- Bull, P.A., 1981. Some fine-grained sedimentation phenomena in caves. *Earth Surf. Process. Landforms* **6**, 11–22.
- Campaña, I., Pérez-González, A., Benito-Calvo, A., Rosell, J., Blasco, R., Bermúdez De Castro, J.M., Carbonell, E., Arsuaga, J.L., 2016. New interpretation of the Gran Dolina-TD6 bearing Homo antecessor deposits through sedimentological analysis. *Sci. Rep.* **6**, 34799. <https://doi.org/10.1038/srep34799>.
- Campaña, I., Benito-Calvo, A., Pérez-González, A., Ortega, A.I., Bermúdez de Castro, J.M., Carbonell, E., 2017. Pleistocene sedimentary facies of the Gran Dolina archaeo-paleoanthropological site (Sierra de Atapuerca, Burgos, Spain). *Quat. Int.* **433**, 68–84.
- Carbonell, E., Rodríguez, X.P., 1994. Early-Middle Pleistocene deposits and artefacts in the Gran Dolina site (TD4) of the Sierra de Atapuerca (Burgos, Spain). *J. Hum. Evol.* **26**, 291–311.
- Carbonell, E., Bermúdez de Castro, J.M., Arsuaga, J.L., et al., 1995. Lower Pleistocene hominids and artifacts from Atapuerca-TD6 (Spain). *Science* **269**, 826–829.
- Carbonell, E., Bermúdez de Castro, J.M., Arsuaga, J.L., Allué, E., Bastir, M., Benito, A., Cáceres, I., Canals, T., Díez, J.C., Van der Made, J., Mosquera, M., Ollé, A., Pérez-González, A., Rodríguez, J., Rodríguez, X.P., Rosas, A., Rosell, J., Sala, R., Vallverdú, J., Vergés, J.M., 2005. An early Pleistocene hominin mandible from Atapuerca-TD6, Spain. *Proc. Natl. Acad. Sci. USA* **102**, 5674–5678.
- Carbonell, E., Bermúdez de Castro, J.M., Parés, J.M., Pérez-González, A., Cuencabescós, G., Olle, A., Mosquera, M., Huguet, R., van der Made, J., Rosas, A., Sala, R., Vallverdú, J., García, N., Granger, D.E., Martín-Torres, M., Rodríguez, X.P., Stock, G.M., Vergés, J.M., Allué, E., Burjachs, F., Cáceres, I., Canals, A., Benito, A., Díez, C., Lozano, M., Mateos, A., Navazo, M., Rodríguez, J., Rosell, J., Arsuaga, J.L., 2008. The first hominin of Europe. *Nature* **452**, 465–470.
- Couchoud, I., 2008. Les spéléothèmes, archives des variations paléoenvironnementales. *Quaternaire* **19** (4), 255–274.
- Cuenca-Bescós, G., Laplana, C., Canudo, J.I., 1999. Biochronological implications of the Arvicidae (Rodentia, Mammalia) from the lower Pleistocene hominin-bearing level of Trinchera Dolina 6 (TD6, Atapuerca, Spain). *J. Hum. Evol.* **37**, 353–373.
- Cuenca-Bescós, G., Blain, H.A., Rofes, J., Lozano-Fernández, I., López-García, J.M., Duval, M., Galán, J., Núñez-Lahuerta, C., 2015. Comparing two different Early Pleistocene microfaunal sequences from the caves of Atapuerca, Sima del Elefante and Gran Dolina (Spain): biochronological implications and significance of the Jaramillo subchron. *Quat. Int.* **389**, 148–158.
- Day, R., Fuller, M.D., Schmidt, V.A., 1977. Hysteresis properties of titanomagnetites: grain size and composition dependence. *Phys. Earth Planet. In.* **13**, 260–266.
- Durcan, J.A., King, G.E., Duller, G.A.T., 2015. DRAC: dose rate and age calculator for trapped charge dating. *Quat. Geochronol.* **28**, 54–61.
- Duval, M., 2012. Dose response curve of the ESR signal of the Aluminum center in quartz grains extracted from sediment. *Ancient TL* **30** (2), 1–9.
- Duval, M., Guilarte Moreno, V., 2012. Assessing the influence of the cavity temperature on the ESR signal of the Aluminum center in quartz grains extracted from sediment. *Ancient TL* **30** (2), 11–16.
- Duval, M., Arnold, L.J., 2013. Field gamma dose-rate assessment in natural sedimentary contexts using LaBr₃(Ce) and NaI(Tl) probes: a comparison between the "threshold" and "windows" techniques. *Appl. Radiat. Isot.* **74** (0), 36–45.
- Duval, M., Sancho, C., Calle, M., Guilarte, V., Peña-Monné, J.L., 2015. On the interest of using the multiple centers approach in ESR dating of optically bleached quartz grains: some examples from the Early Pleistocene terraces of the Alcandre River (Ebro basin, Spain). *Quat. Geochronol.* **29**, 58–69.
- Duval, M., Arnold, L.J., Guilarte, V., Demuro, M., Santonja, M., Pérez-González, A., 2017. Electron spin resonance dating of optically bleached quartz grains from

- the Middle Palaeolithic site of Cuesta de la Bajada (Spain) using the multiple centres approach. *Quat. Geochronol.* 37, 82–96.
- Falguères, C., Bahain, J.J., Yokoyama, Y., Arsuaga, J.L., Bermúdez de Castro, J.M., Carbonell, E., Bischoff, J.L., Dolo, J.M., 1999. Earliest humans in Europe: the age of TD6 gran Dolina, Atapuerca, Spain. *J. Hum. Evol.* 33, 343–352.
- Ford, D., Williams, 2007. Karst Hydrogeology and Geomorphology. John Wiley & Sons, Ltd.
- Frank, N., Kober, B., Mangini, A., 2006. Carbonate precipitation, U-series dating and U-isotopic variations in a Holocene travertine platform at Bad Langensalza - Thuringia Basin, Germany. *Tufs calcaires et travertins quaternaires: morphogénèse, biocénoses, paléoclimats et implantations paléolithiques. 2ème partie. Quaternaire* 17 (4), 333–342 (2006).
- García, N., Arsuaga, J.L., Torres, T., 1997. The carnivore remains from the Sima de los Huesos Middle Pleistocene site (Sierra de Atapuerca, Spain). *J. Hum. Evol.* 33, 155–174.
- Gradstein, F.M., Ogg, J.G., Schmitz, M.D., Ogg, G.M. (Eds.), 2012. The Geologic Time Scale 2012, vol. 1. Elsevier, p. 144.
- Grün, R., 1994. A cautionary note: use of the water content and depth for cosmic ray dose rate in AGE and DATA programs. *Ancient TL* 12, 50–51.
- Guérin, G., Mercier, N., Adamiec, G., 2011. Dose-rate conversion factors: update. *Ancient TL* 19 (1), 5–8.
- Guérin, G., Mercier, N., Nathan, R., Adamiec, G., Lefrais, Y., 2012. On the use of the infinite matrix assumption and associated concepts: a critical review. *Radiat. Meas.* 47 (9), 778–785.
- Harmand, D., Adamson, K., Rixhon, G., Jailliet, S., Losson, B., Devos, A., Hez, G., Calvet, M., Audra, P., 2017. Relationships between fluvial evolution and karstification related to climatic, tectonic and eustatic forcing in temperate regions. *Quat. Sci. Rev.* <https://doi.org/10.1016/j.quascirev.2017.02.016>.
- Jelinek, V., 1978. Statistical processing of anisotropy of magnetic susceptibility measured on groups of specimens. *Studia Geophys. et geol.* 22, 50–62.
- Jelinek, V., 1981. Characterization of the magnetic fabric of rocks. *Tectonophysics* 79, 63–67.
- Moreno, D., Falguères, C., Pérez, A., Voinchet, P., Ghaleb, B., Despriée, Bahain, J.J., Sala, R., Carbonell, E., Bermúdez de Castro, J.M., Arsuaga, J.L., 2015. New radiometric dates on the lowest stratigraphical section (TD1 to TD6) of Gran Dolina site (Atapuerca, Spain). *Quat. Geochronol.* 30, 535–540.
- Nagata, T., 1961. Rock Magnetism. Maruzen, Tokyo, p. 350.
- Nye, J.F., 1957. The Physical Properties of Crystals. Clarendon Press, Oxford, p. 322.
- Ollé, A., Mosquera, M., Rodríguez, X.P., de Lomba-Hermida, A., García-Antón, M.D., García-Medrano, P., Peña, L., Menéndez, L., Navazo, M., Terradillos, M., Bargalló, o, A., Márquez, B., Sala, R., Carbonell, E., 2013. The Early and Middle Pleistocene technological record from Sierra de Atapuerca (Burgos, Spain). *Quat. Int.* 295, 138–167.
- Ortega, A.I., Benito-Calvo, A., Pérez-González, A., Martín-Merino, M.A., Pérez-Martínez, R., Pares, J.M., Aramburu, A., Arsuaga, J.L., Bermúdez de Castro, J.L., Carbonell, E., 2013. Evolution of multilevel caves in the Sierra de Atapuerca (Burgos, Spain) and its relation to human occupation. *Geomorphology* 196, 122–137.
- Ortega, A.I., Benito-Calvo, A., Pérez-González, A., Arsuaga, J.L., Bermúdez de Castro, J.L., Carbonell, E., 2014. Atapuerca karst and its palaeoanthropological sites. In: Gutiérrez, F., Gutiérrez, M. (Eds.), Landscapes and Landforms of Spain, World Geomorphological Landscapes. Springer Science+Business Media Dordrecht 2014, pp. 101–111.
- Parés, J.M., Pérez-González, A., 1995. Paleomagnetic age for hominid fossils at Atapuerca Archaeological site, Spain. *Science* 269, 830–832.
- Parés, J.M., Hassold, N.J.C., Rea, D.K., van der Pluijm, B.A., 2007. Paleocurrent directions from paleomagnetic reorientation of magnetic fabrics in deep-sea sediments at the Antarctic Peninsula Pacific margin (OPD Sites 1095, 1101). *Mar. Geol.* 242, 261–269.
- Parés, J.M., Pérez-González, A., Arsuaga, J.L., Bermúdez de Castro, J.M., Carbonell, E., Ortega, A., 2010. Characterizing sedimentary history of cave deposits, using archaeomagnetism and rockmagnetism, Atapuerca (N Spain). *Archaeometry* 52 (5), 882–898.
- Parés, J.M., Lee, A., Duval, M., Demuro, D., Pérez-González, A., Bermúdez de Castro, J.M., Carbonell, E., Arsuaga, J.L., 2013. Reassessing the age of Atapuerca TD-6 (Spain): new paleomagnetic data. *J. Archaeol. Sci.* 40, 4586–4595.
- Parés, J.M., Ortega, A.I., Benito-Calvo, A., Aramburu, A., Arsuaga, J.L., Bermúdez de Castro, J.M., Carbonell, E., 2016. Paleomagnetic constraints on the Atapuerca karst development (N Spain). In: Feinberg, J., Gao, Y., Alexander Jr., E.C. (Eds.), Caves and Karst across Time: Geological Society of America Special Paper 516, pp. 285–300. [https://doi.org/10.1130/2016.2516\(22\)](https://doi.org/10.1130/2016.2516(22)).
- Paton, C., Hellstrom, J., Paul, B., Woodhead, J., Hergt, J., 2011. Iolite: freeware for the visualisation and processing of mass spectrometric data. *J. Anal. At. Spectrom.* 26 (12), 2508–2518.
- Prescott, J.R., Hutton, J.T., 1994. Cosmic ray contributions to dose rates for luminescence and ESR dating: large depths and long-term time variations. *Radiat. Meas.* 23, 497–500.
- Rossi, C., Villalain, J.J., Lozano, R.P., Hellstrom, J., 2016. Paleo-watertable definition using cave ferromanganese stromatolites and associated cave-wall notches (Sierra de Arnero, Spain). *Geomorphology* 57–75.
- Singer, B.S., 2014. A Quaternary geomagnetic instability time scale. *Quat. Geochronol.* 21, 29–52.
- Schmitz, M.D., Schoene, B., 2007. Derivation of isotope ratios, errors, and error correlations for U-Pb geochronology using 205Pb-235U-(233U)-spiked isotope dilution thermal ionization mass spectrometric data. G-cubed. <https://doi.org/10.1029/2006GC001492>.
- Stacey, F.D., Joplin, G., Lindsay, J., 1960. Magnetic anisotropy and fabric of some foliated rocks from SE Australia. *Geophysica Pura Appl.* 47, 551–556.
- Tarling, D.H., Hrouda, F., 1993. The Magnetic Anisotropy of Rocks. Chapman and Hall, London, p. 217.
- Tauxe, L., 1993. Paleomagnetic Principles and Practice. Kluwer Academic Publishers, Dordrecht, p. 297.
- Vandenbergh, D., De Corte, F., Buylaert, J.P., Kucera, J., Van den haute, P., 2008. On the internal radioactivity in quartz. *Radiat. Meas.* 43, 771–775.
- Woodhead, J., Hellstrom, J., Pickering, R., Drysdale, R., Paul, B., Bajío, P., 2012. U and Pb variability in older speleothems and strategies for their chronology. *Quat. Geochronol.* 14, 105–113.
- Woodhead, J., Hellstrom, J., Maas, R., Drysdale, R., Zanchetta, G., Devine, P., Taylor, E., 2006. U-Pb geochronology of speleothems by MC-ICPMS. *Quat. Geochronol.* 1, 208–221.
- Yokoyama, Y., Falgueres, C., Quaegebeur, J.P., 1985. ESR dating of quartz from quaternary sediments: first attempt. *Nucl. Tracks Radiat. Meas.* 10 (4–6), 921–928.
- Zijderveld, J.D.A., 1967. AC demagnetization of rocks: analysis of results. In: Collinson, D.W., Runcorn, S.K., Creer, K.M. (Eds.), Methods in Paleomagnetism. Elsevier, New York, pp. 254–286.